Geothermics 104 (2022) 102451

Contents lists available at ScienceDirect

Geothermics

journal homepage: www.elsevier.com/locate/geothermics

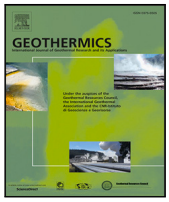

A seismic-properties and wave-propagation analysis for the long-term monitoring of supercritical geothermal systems

Biancamaria Farina [a,*], Francesco Parisio [b,c,d], Flavio Poletto [a]

[a] Istituto Nazionale di Oceanografia e di Geofisica Sperimentale - OGS, Borgo Grotta Gigante 42/C, 34010 Sgonico, Trieste, Italy
[b] Institute of Environmental Assessment and Water Research (IDAEA), Spanish National Research Council (CSIC), Carrer de Jordi Girona, 18-26, 08034 Barcelona, Spain
[c] Mediterranean Institute for Advanced Studies (IMEDEA), Spanish National Research Council (CSIC), Carrer de Miquel Marquès, 21, 07190 Esporles, Illes Balears, Spain
[d] Associated Unit: Hydrogeology Group UPC-CSIC, Carrer de Jordi Girona, 18-26, 08034 Barcelona, Spain

ARTICLE INFO

Keywords:
Geothermal reservoir
Supercritical fluid
Seismic properties
Burgers–Gassmann model
Long-term injection
Time-lapse seismic monitoring

ABSTRACT

This study is focused on the modeling of the seismic response in a supercritical geothermal system subjected to a long-term cold and isothermal re-injection during 20 years of exploitation. The modeling aims to assess the usability of seismic-methods for monitoring supercritical geothermal reservoir. We use a synthetic data set for the analysis of the seismic properties of the reservoir: pressure and temperature evolution is derived from a previous numerical study of a two-dimensional supercritical reservoir with pure water as the pore fluid. We calculate the related variations in time of the seismic properties of the reservoir saturated-rock formation using the Burgers–Gassmann mechanical model to evaluate the effects of high temperature on the rock frame, and to account for fluid-properties variations. We observe that, at the analyzed pressure and temperature conditions, the seismic properties of the reservoir formation are mainly determined by the thermophysical characteristics of the pore fluid. During the long-term cold re-injection we observe a decrease in the compressional seismic velocity in the cooled area near the injection well, with a radius that increases in time. We use a 2D full-waveform propagation algorithm based on the Burgers–Gassmann model to calculate synthetic signals in a single-well acquisition layout, with a time step of half year. We observe that in the cool injection scenario the changes in the anomalous area can be seismically monitored, while in the case of isothermal injection, changes due to the re-injection are not seismically appreciable.

1. Introduction

Supercritical geothermal systems have recently attracted attention as a challenging type of unconventional high-temperature geothermal resources, usually associated with shallow magmatic intrusions, since they could provide significantly higher well productivities with respect to wells drilled in classic hydrothermal systems (de Franco et al., 2019). The heat capacity of supercritical fluids, that directly impacts energy production, is much higher than that of fluids at subcritical conditions (Elders et al., 2014). Supercritical geothermal systems are frequently located at depths near or below the brittle–ductile transition (BDT) zone in the crust (Parisio et al., 2020) where the reservoir fluid is typically assumed to be in the supercritical state. Recent studies (e.g., Watanabe et al., 2017, 2021) have demonstrated that near the BDT the permeability is sufficient to allow fluid circulation, and that the BDT does not exert the first-order control on rock permeability. Therefore, potentially exploitable geothermal resources may occur in crystalline rocks, like those that characterize the continental crust, where it would be possible to develop enhanced supercritical geothermal systems (ESGS).

The stage of exploration is important for the reduction of risks in the development of a geothermal field and during its exploitation (Elders et al., 2014), and for the achievement of the advances in geothermal energy utilization. Seismic reservoir characterization and monitoring is important in integrated exploration of geothermal reservoirs. One valuable tool for a geothermal reservoir development and monitoring is the computer simulation of its response to wave propagation. Several works have been presented on geophysical analysis and numerical simulations, in addition to other methods, aimed to improve the characterization and imaging of geothermal reservoirs in the presence of supercritical fluids and near the BDT (e.g., Reinsch et al., 2017; Jusri et al., 2019). Carcione and Poletto (2013) considered deformation by shear plastic flow with temperature in the crust and proposed

* Corresponding author.
E-mail address: bfarina@ogs.it (B. Farina).

https://doi.org/10.1016/j.geothermics.2022.102451
Received 13 January 2022; Received in revised form 5 May 2022; Accepted 6 May 2022
Available online 26 May 2022

an elastic–plastic rheology including the effects of crust anisotropy, seismic attenuation and ductility. They used the Burgers mechanical model with the octahedral stress criterion and the Arrhenius equation to include the temperature, and to describe the effects of seismic attenuation, velocity dispersion, and steady-state creep flow. Carcione et al. (2014) presented a simulation algorithm based on the Burgers model for waveform propagation in rock frames where deformation takes place by shear plastic flow. Gurevich et al. (2009) studied the seismic attenuation and dispersion in hydrocarbon reservoir and described the effects of changes in pore fluids on the rock bulk modulus. Jaya et al. (2010) performed petrophysical experiments on geothermal rocks, and used Gassmann's equation as a predictive model for seismic velocity. They assumed the independence of the grain and dry-rock moduli from the temperature, applying their analysis to a range of temperatures where melting does not occur. Carcione et al. (2017) extended the study of rock deformation due to shear plastic flow at high temperature to poro-viscoelastic media using the Gassmann's equation to explicitly model the effects of pore fluids and to predict the seismic properties of saturated rocks. They obtained PS and SH equations corresponding to isotropic anelastic and inhomogeneous media and presented the Burgers–Gassmann simulation algorithm obtained by solving a direct grid method based on the Runge–Kutta time stepping technique and the Fourier pseudospectral method.

During the geothermal reservoir exploitation, changes in the pore pressure and temperature conditions caused by production or injection induce variations in the fluid properties and also fluid phase transition that can lead to time variations in seismic velocities and attenuation (Jaya et al., 2010). In this work, we use the Burgers–Gassmann mechanical (BGM) model and simulation code (Carcione et al., 2017) to analyze the influence of temperature on the seismic properties of the fluid-saturated rocks in a supercritical geothermal reservoir, in which we focus the analysis on prolonged fluid re-injection, and assume that a successful stimulation took place in the surroundings of the well. We consider two cases analyzed in the literature (Parisio et al., 2019): the first is an extreme cooling scenario where the cold re-injection produces very large thermal stress variations associated to a significant temperature drop; the second is an isothermal re-injection, where the temperature almost unaltered. We evaluate the related variations in the saturated rock. We simulate the seismic response in the case of a single-well (SW) acquisition with the source and receiver in the same well (Hornby, 1989; Chabot et al., 2001; Poletto et al., 2011) during the reservoir exploitation. The study demonstrates that, at the analyzed pressure and temperature conditions, the seismic properties of the rock frame are not temperature dependent and that the saturated rock properties depend mostly on the thermophysical characteristics of the saturating fluid. This result is clearly observable in the extreme cooling scenario, where the effect of long-term exploitation can be highlighted by seismic monitoring.

2. Theory and methods

2.1. Thermo-hydro-mechanical model

The input data of the seismic model consists of the results from a previous thermo-hydro-mechanical (THM) modeling study on the behavior of supercritical geothermal systems during long-term re-injection, where pure water is considered as saturating fluid (Parisio et al., 2019). Here, we briefly report the field equations that were solved using the finite element method to produce the synthetic database, while we address the reader to the original work of Parisio et al. (2019) for more details. The database that forms the input of the seismic model is constructed by solving the transient and coupled problem of pressure, temperature and displacement evolution in porous media with the open-source finite element solver OpeGeoSys (Kolditz et al., 2012). The THM problem in the porous medium is governed by the non-linear system of partial differential equations that describe the balance of mass, energy and momentum. The unknowns of the problem describe the evolution in time t of the fields of pore pressure p, temperature T and displacement $\mathbf{u}$ (Parisio et al., 2019). In the following, subscripts 's' and 'f' stand for solid and fluid, respectively. The mass balance equation writes

$$S_{\rm m}\frac{{\rm d}_s p}{{\rm d}t} - \Gamma_T \frac{{\rm d}_s T}{{\rm d}t} - \nabla\cdot\mathbf{v}_{\rm m} + \alpha\nabla\cdot\frac{{\rm d}_s\mathbf{u}}{{\rm d}t} = Q_{\rm H}, \tag{1}$$

where $S_{\rm m} = \phi\beta_{\rm f} + \frac{\alpha-\phi}{K_{\rm s}}$ is the storage coefficient, ϕ is the porosity, $\beta_{\rm f}$ is the fluid's compressibility, $\alpha = 1 - K/K_{\rm s}$ is Biot's coefficient, K is the drained bulk modulus and $K_{\rm s}$ is the bulk modulus of the solid phase. The term $\Gamma_T = \phi\alpha_{\rm f} + 3\alpha_{\rm s}(\alpha-\phi)$ represents the thermal pressurization, i.e., the differential thermal expansion between the fluid $\alpha_{\rm f}$ and the porous solid α_s.

The term $\mathbf{v}_{\rm m} = \frac{\mathbf{k}}{\mu_{\rm f}}(\nabla p - \rho_{\rm f}\mathbf{g})$ is the Darcy's velocity and is a function of the permeability tensor $\mathbf{k}$, the dynamic viscosity $\mu_{\rm f}$, the fluid density $\rho_{\rm f}$ and the gravity acceleration vector $\mathbf{g}$. $Q_{\rm H}$ is a source term of the hydraulic problem.

The energy balance equation takes the form

$$C_{\rm m}\frac{{\rm d}_s T}{{\rm d}t} - \nabla\cdot\left(\Lambda_{\rm m}\nabla T\right) - \rho_{\rm f}c_{\rm f}\mathbf{v}_{\rm m}\cdot\nabla T = Q_{\rm T}, \tag{2}$$

where $C_{\rm m} = \phi\rho_{\rm f}c_{\rm f} + (1-\phi)\rho_{\rm s}c_{\rm s}$ and $\Lambda_{\rm m} = \phi\lambda_{\rm f}\mathbf{I} + (1-\phi)\lambda_{\rm s}$ are the heat capacity and thermal conductivity of the porous medium, respectively. For the solid phase representing the host rock, $\rho_{\rm s}$ is the mass density, $c_{\rm s}$ is the specific heat capacity and $\lambda_{\rm s}$ is the thermal conductivity. $Q_{\rm T}$ is a source term for the energy balance problem. The linear momentum balance equation is

$$\left(K + \frac{G}{3}\right)\nabla\left(\nabla\cdot\mathbf{u} - 3\alpha_{\rm s}\Delta T\right) + 3K\nabla^2\mathbf{u} - \nabla\cdot(\alpha p\mathbf{I}) + \rho_{\rm m}\mathbf{g} = \mathbf{0}, \tag{3}$$

where the density of the porous medium is $\rho_{\rm m} = \phi\rho_{\rm f} + (1-\phi)\rho_{\rm s}$, G is the shear modulus of the porous medium and $\mathbf{I}$ is the identity tensor.

2.2. Burgers-Gassmann mechanical model

To study the seismic response of the supercritical geothermal reservoir during operational conditions we use the BGM model, to describe the anelastic behavior of the porous rock due to shear deformation and plastic flow (Carcione and Poletto, 2013; Carcione et al., 2014). The frequency-dependent Burgers complex shear modulus is given by

$$G_{\rm B} = \frac{G_0(i\omega\tau_\epsilon + 1)}{i\omega\tau_\sigma + 1 - \frac{iG_0}{\omega\eta_{\rm s}}(i\omega\tau_\epsilon + 1)}, \tag{4}$$

where ω in the angular frequency, $i = \sqrt{-1}$, G_0 is the relaxed shear modulus of the Zener element, that describes the brittle material behavior (Carcione et al., 2006, 2014). The seismic relaxation times for shear deformations τ_ϵ and τ_σ are

$$\tau_\epsilon = \frac{1}{\omega_0 Q_0}\left(1 + \sqrt{Q_0^2 + 1}\right), \quad \tau_\sigma = \tau_\epsilon - \frac{2}{\omega_0 Q_0}, \tag{5}$$

where Q_0 is the minimum quality factor, which can be obtained from the experimental relaxation times and ω_0 is the center frequency of the relaxation peak (Carcione et al., 2006). The effective shear viscosity ($\eta_{\rm s}$) can be expressed by the constitutive creep law trough the Arrhenius equation for the temperature dependence

$$\eta_s = \frac{\tau_{oct}^{1-n}}{2A_0}\exp(E/RT), \tag{6}$$

where τ_{oct} is the shear octahedral stress, A_0 is a material constant, n is the stress exponent, that characterizes the sensitivity of strain rate on the differential stress, E is the activation energy, $R = 8.3144$ J/mol/K is the Boltzmann's gas constant and T is the absolute temperature (e.g., Carcione et al., 2017; Montési, 2007). The flow parameters A_0 and n are determined in the laboratory tests on rock rheology at

different strain rates, temperatures and/or stresses (e.g., Gangi, 1983). The octahedral shear stress is expressed by

$$\tau_{oct} = \frac{1}{3}[(\sigma_{xx} - \sigma_{yy})^2 + (\sigma_{xx} - \sigma_{zz})^2 + (\sigma_{zz} - \sigma_{yy})^2 + 6(\sigma_{xy}^2 + \sigma_{xz}^2 + \sigma_{yz}^2)]^{1/2}, \tag{7}$$

where σ_{ij} $(i = j)$ are the normal stresses and σ_{ij} $(i \neq j)$ are the shear stresses acting in the j direction on a plane normal to the i direction. The physical mechanism behind the Arrhenius equation is the grain-boundary relaxation (Carcione et al., 2020).

We use the Gassmann's theory to predict the change, in the low-frequency approximation, of the undrained stiffness caused by replacing or substituting the pore fluids within a rock. From the assumptions used to derive the Gassmann's equation, it results that the saturated rock shear modulus is independent on pore fluid (Berryman, 1999). Shear deformation does not produce a pore-volume change, and consequently different fluid properties do not affect the shear modulus, and any fluid-saturation effect should correlate mainly to a change in the bulk modulus (Han and Batzle, 2004). The fluid-saturated bulk and shear moduli ($K_{\rm sat}$ and $\mu_{\rm sat}$) are given by

$$K_{\rm sat} = K + \alpha^2 \left[\frac{K_{\rm s}}{\alpha - \phi + \phi \frac{K_{\rm s}}{K_{\rm f}}} \right], \tag{8}$$

and

$$G_{\rm sat} = G_{\rm B}, \tag{9}$$

respectively. $K_{\rm f}(T, p)$ is the fluid bulk modulus which is a function of the reservoir temperature (T) and pore pressure (p) conditions. The complex, frequency dependent seismic compressional (P) and shear (S) velocities of the saturated rocks are

$$c_{\rm P} = \sqrt{\frac{K_{\rm sat} + 4G_{\rm sat}/3}{\rho_{\rm m}}} \quad \text{and} \quad c_{\rm S} = \sqrt{\frac{G_{\rm sat}}{\rho_{\rm m}}}. \tag{10}$$

For homogeneous waves in isotropic media, the phase velocity and quality factors are

$$V_i = \left[{\rm Re} \left\{ \frac{1}{c_i} \right\} \right]^{-1}, \quad \text{and} \quad Q_i = \frac{{\rm Re}\{c_i^2\}}{{\rm Im}\{c_i^2\}}, \quad (i = P, S), \tag{11}$$

respectively. The theory allows us to obtain compressional and shear phase velocities and quality factors as functions of depth, stress and temperature as well as frequency.

To calculate the synthetic waveform propagation we use a 2D simulation algorithm based on the BGM model, the Arrhenius equation and the octahedral stress criterion (Carcione et al., 2017). The PS and SH equations of motion have been recasted in the velocity–stress formulation, including memory variables to avoid the computation of time convolutions. The equations correspond to isotropic anelastic and inhomogeneous media and are solved by a direct grid method based on the Runge–Kutta time stepping technique and the Fourier pseudospectral method for the spatial derivatives. The resulting derivative approximation is highly accurate and requires fewer grid points to achieve comparable accuracy to that of finite difference or finite element methods (Kosloff et al., 1984; Fornberg, 1987). The code was tested against known analytical solutions for different values of shear viscosity (Carcione et al., 2017), it was used for waveform simulation in heterogeneous model including melting (Poletto et al., 2019b) and benchmarked with viscoelastic code (Poletto et al., 2019a).

3. Examples

The results of the THM analysis carried out by Parisio et al. (2019) are the input data used here to study the seismic response of the supercritical geothermal reservoir during operational conditions.

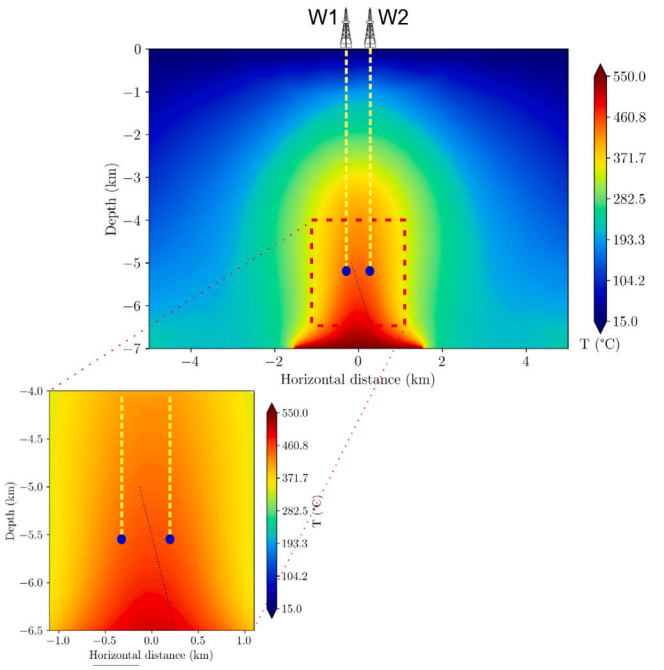

Fig. 1. Temperature model of the supercritical geothermal system at initial time, when the reservoir exploitation starts. The yellow lines indicates the positions of the extraction well (W1) and the injection well (W2). The blue dashed line indicates the fault position. The red dashed lines show the sub-area analyzed during the reservoir exploitation which is represented in the small panel below. (For interpretation of the references to color in this figure legend, the reader is referred to the web version of this article.)

3.1. Models properties

The model for the THM and the seismic analyses consists of a 10 km-wide and 7 km-deep reservoir composed of a homogeneous background medium with drained bulk modulus $K = 40$ GPa, shear modulus $G = 24$ GPa, Biot's coefficient $\alpha = 0.5$, porosity $\phi = 0.01$, solid phase bulk modulus and density $K_{\rm s} = 80$ GPa and $\rho_{\rm s} = 2700$ kg m^{-3}, respectively. The model includes a production (W1) and an injection (W2) well at horizontal positions −250 m and +250 m, respectively, geologically separated by a 1 m thick sub-vertical fault. For the fault we have assumed different properties from those of the host rock, namely, $\phi = 0.05$, $K = 13.3$ GPa, $G = 8$ GPa, and $\alpha = 1.0$. The porosity of the host rock nearby the fault increases gradually. Fig. 1 shows the temperature model of the geothermal reservoir at the initial exploitation time, with superimposed the scheme of the two wells (yellow dashed lines) and the fault (blue dashed line).

Without loss of generality, pure water is considered as saturating fluid. The fluid's compressibility and thermal expansion coefficients are computed through perturbation of the equation of state of water, which follows the IAPWS-IF97 standard and is computed via link to the freesteam library.[1] Accordingly, the library is used to compute the water properties, such as the dynamic viscosity $\mu_{\rm f}$, the density $\rho_{\rm f}$, the acoustic velocity used to calculate the bulk modulus $K_{\rm f}$, the specific heat capacity $c_{\rm f}$ and the thermal conductivity $\lambda_{\rm f}$.

The porous solid specific heat capacity, linear thermal expansion coefficient and thermal conductivity are $c_{\rm s} = 950$ J kg^{-1} K^{-1}, $\alpha_{\rm s} = 1 \cdot 10^{-5}$ K^{-1} and $\lambda_{\rm s} = 3\mathbf{I}$ W m^{-1} K^{-1}, respectively. To analyze the dependence of the seismic properties of the host rock on the temperature we consider the Arrhenius parameters, appearing in the constitutive creep law (Eq. (6)), that are experimentally derived by Violay et al. (2012)

[1] Available at http://freesteam.sourceforge.net/.

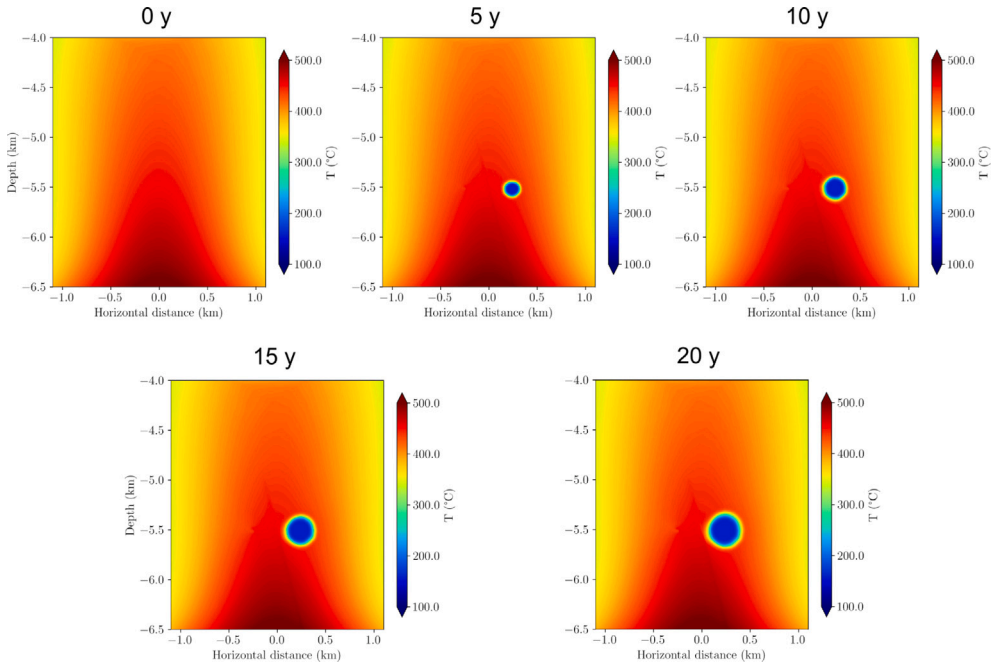

Fig. 2. Temperature models with 5-years step during 20 years of cold re-injection.

for the glassy basalt samples. We use the stress exponent $n = 3.7$, the activation energy $E = 59$ kJ/mol and the coefficient $A_0 = A \cdot (3^{(n+1)/2}/2)$ where $A = 1.3 \cdot 10^{-9}$ (MPa^{-n}/s) is determined from laboratory creep experiments and the geometric factor in brackets takes into account the conversion from the creep laboratory data (Ranalli, 1995). The relaxation times in Eqs. (5) are calculated by using as minimum quality factor the shear seismic loss parameter derived by Castro et al. (2008) for the crust in Southern Italy, $Q_0 = 18.8\ f_0^{1.7}$, with $f_0 = 3$ Hz.

3.2. Analysis of seismic properties

Starting from the results of Parisio et al. (2019) we calculate the saturated rock compressional and shear phase velocities during 20 years of re-injection by taking into account the variations of pore pressure, geothermal fluid properties, stress and temperature conditions. We focus the analysis on the small area, that is most affected by the re-injection process, 2 km deep, 2.5 km wide, centered around the fault and evidenced in the lower panel of Fig. 1. We extract a sub-sect from the data obtained with the THM simulation, distributed on an unstructured grid with a refinement near the wells, without changing the discretization. We analyze two possible scenarios that represent different extreme behaviors: a case in which the fluid is reinjected at a much lower temperature than the reservoir (cold re-injection), and a case in which the fluid is reinjected at the same temperature of the reservoir (isothermal re-injection).

Temperature and pressure conditions in the geothermal reservoir strongly affect the thermophysical characteristics of the pore fluid and can also affect the seismic properties of the drained rock frame. Moreover, high temperature and pressure conditions can allow the presence of melted material with a consequent decrease of the rock frame viscosity (e.g. Poletto et al., 2018; Farina et al., 2019). Viscosity lower than 10^{11} Pa s are associated to the presence of melting and this significantly affects the compressional and shear velocities and attenuations (Mavko, 1980; Solomon, 1972; Farina et al., 2019). We calculate the shear viscosity of the host rock frame at the temperature and pressure conditions near the injection bottom-hole well. At the initial time, when the reservoir conditions are the same for the two considered scenarios, and the background temperature is the highest, the shear viscosity is $2 \cdot 10^{14}$ Pa s. This value is greater then that expected for the presence of melting, which could strongly affect the rock shear modulus. Therefore, we can attribute the saturated-rock seismic properties variations, during the reservoir exploitation, mainly to the thermophysical characteristics of the pore fluid. These characteristics strongly affect the temperature dependence of velocity in fluid-saturated rocks (Batzle and Wang, 1992) and in particular of the compressional velocity.

3.2.1. Cold re-injection scenario

Fig. 2 shows the changes in the temperature model with 5-years step in the cold re-injection case. A cooled area, that grows over time, is visible around the position of the well W2 (+250 m), where the cold water is reinjected during the exploitation. Fig. 3 shows the P-wave velocity (V_P) models, of the saturated-rock formation, calculated every five years. A velocity decrease is visible in correspondence of the cooled area shown in Fig. 2. According to the Gassmann's relation (Eq. (9)), the shear modulus of the saturated rock does not depend on the pore fluid properties, and the shear-wave velocity is related to the fluid only through the density of the porous medium (Eq. (10)). The saturated rock S-wave velocity (V_S) is almost independent on the temperature variation, as shown in Fig. 4 where only the models at initial time and after 20 years of re-injection are replotted. To better understand how the variations of the conditions related to the re-injection affects the seismic properties of the saturated reservoir formation, we extract a 1D horizontal line at the bottom-hole depth, 5.5 km, where the maximum changes are observed. Figs. 5a and b show the variations of the temperature and pore pressure in the reservoir with 5-years step. The radius of the cooled area grows of about 120 m in the first five years, half of which in the first year, than the rate of expansion decreases down to about 10 m/year. The cold injection induces a drop of temperatures of about 300 °C and an increase of the pore pressure of 4 – 7 GPa in 20 years. The points of extraction and re-injection are visible in the drop and the increase of pore pressure near the production W1 (−250 m) and the extraction W2 (+250 m) wells, respectively. Fig. 5c shows the variation of the fluid density in the same period. The density increases from about 400 kg/m^3 to more than 900 kg/m^3 corresponds to a change in the fluid conditions, from supercritical to liquid phase. Fig. 5d, e and f show the compressional- and shear-wave velocity and the ratio V_P/V_S of the saturated host rock. The slight

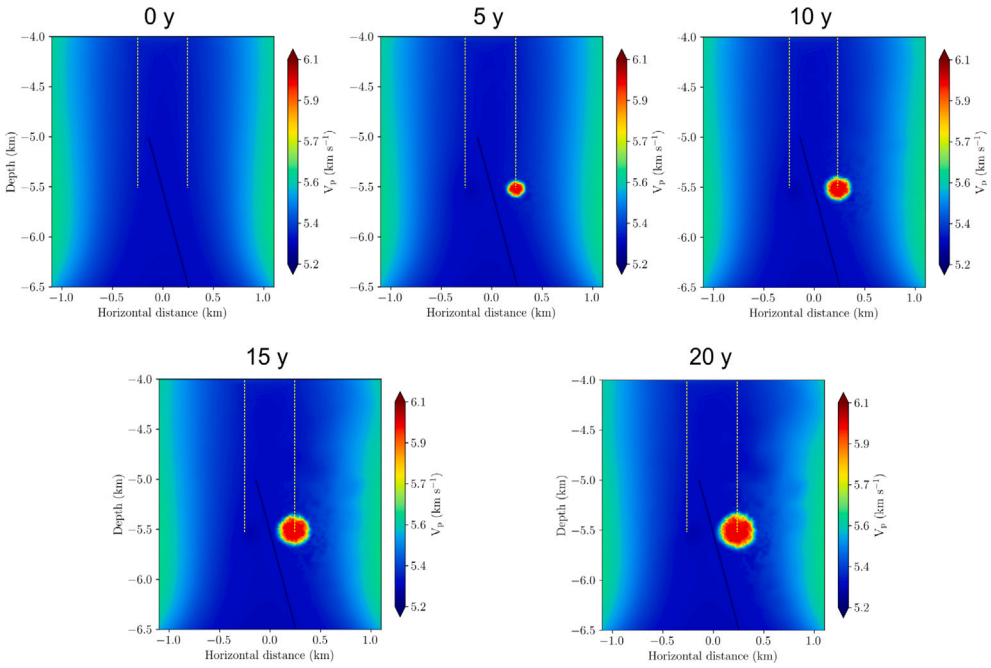

Fig. 3. Compressional phase-velocity models with 5-years step during 20 years of cold re-injection. Yellow lines indicate the position of the wells. (For interpretation of the references to color in this figure legend, the reader is referred to the web version of this article.)

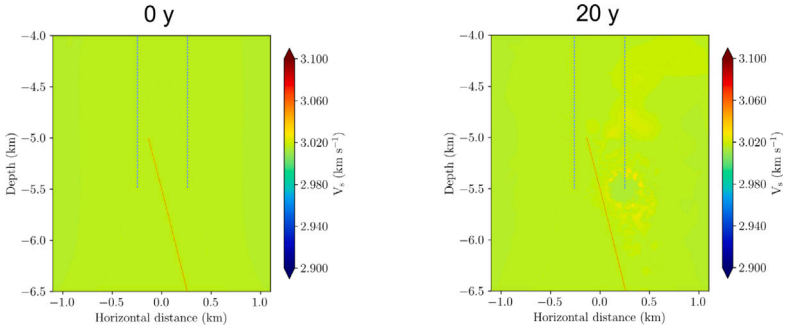

Fig. 4. Shear phase-velocity models at initial time and after 20 years of cold re-injection. Yellow lines indicate the position of the wells. (For interpretation of the references to color in this figure legend, the reader is referred to the web version of this article.)

increase of the S-wave velocity in the proximity of the fault, where V_S decreases with respect to the background, which is observed at every time step (Fig. 5e) is caused by the increase of the porosity of the host rock in the proximity of the fault. The change in the thermophysical properties of the pore fluid near the injection well corresponds to an increase of about 0.7 km/s in V_P. and slightly increase of less than 0.008 km/s of V_S, as shown by the small variations nearby the injection well in Fig. 5e. Fig. 6 shows the crossplots of fluid density and V_P versus temperature and V_P versus fluid density calculated at initial time and after 20 years along the horizontal direction, as reported in the color bar. It is possible to observe how the highest variations are mainly localized in the area of the injection well (yellow points), where the cooling induces the increase of the fluid density and the following increase of the formation compressional-wave velocity. Smaller fluctuations are visible in the area of the production well (red points) where the decrease of pore pressure due to the production induces a decrease of the fluid density and a slight decrease of the V_P.

3.2.2. Isothermal re-injection scenario

In the case of isothermal re-injection, where the downhole injection temperature difference is null ($\Delta T = 0$), variations of the temperature and, therefore, of the wave velocity, are lower with respect the previous scenario. Temperature does not decrease below 400 °C near the wells entailing the absence of phase change for the geothermal pore fluid and very small changes of its seismic properties.

Fig. 7 shows the changes in the temperature model with 5-years step. Only a small temperature reduction affects a slightly visible area near the bottom-hole wells, which grows in time. Fig. 8 shows the changes of the saturated formation P-wave velocity in correspondence of the temperature variations. There are no observable variations in the S-wave velocity. Fig. 9 shows the 1D profiles of the reservoir temperature (Fig. 9a), pore pressure (Fig. 9b), fluid density (Fig. 9c), saturated host rock P- and S-wave velocities (Fig. 9d and e) and V_P/V_S ratio (Fig. 9f), extracted along the horizontal line crossing the bottom-hole wells, at 5.5 km depth. Also in this case, the increase of the host rock porosity in the proximity of the fault, at the horizontal distance 0 km, causes a small increase in the S-wave velocity and a little decrease in the P-wave velocity (Fig. 9e and d, respectively). Fluctuations of few degrees are visible in the temperature model near the bottom hole and result in variations of the P-wave velocity of the order of 0.5% near the production well and smaller in proximity of the injection well, while, as expected, no changes are observable for the S-wave velocity. These results are evidenced in the crossplots of Fig. 10, where fluid density and formation P-wave velocity versus temperature and V_P versus ρ_{fl} are calculated along the horizontal direction at the initial time and after 20 years of injection. The most evident changes are

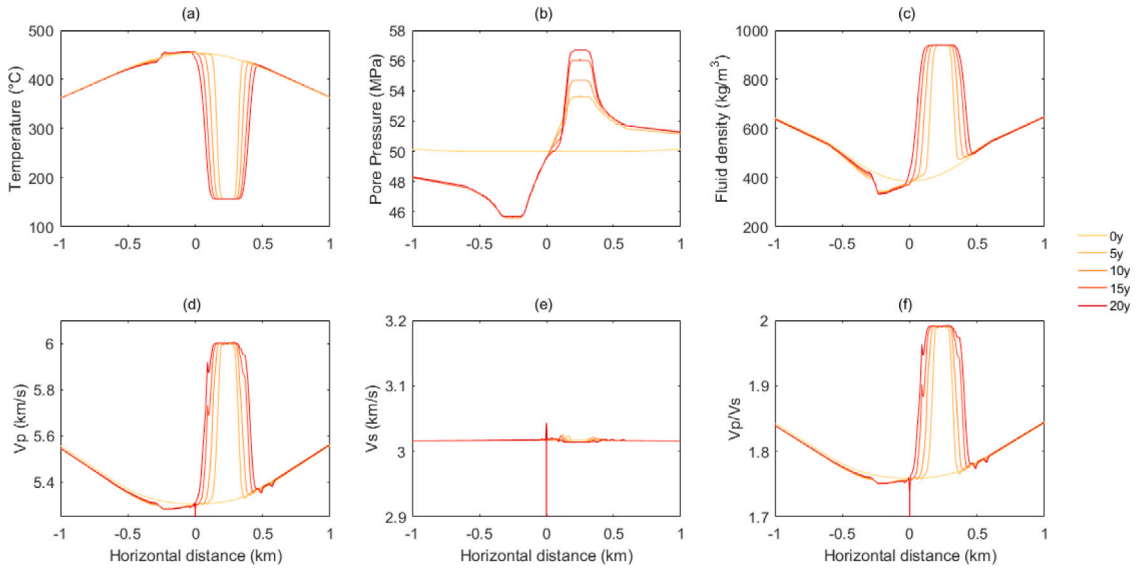

Fig. 5. 1D profiles of (a) temperature, (b) pore pressure, (c) pore-fluid density, saturated rock (d) compressional and (e) shear wave velocities and (f) V_P/V_S ratio, extracted along the horizontal line at the bottom-hole depth, 5.5 km. The data are calculated every 5 years during the cold re-injection.

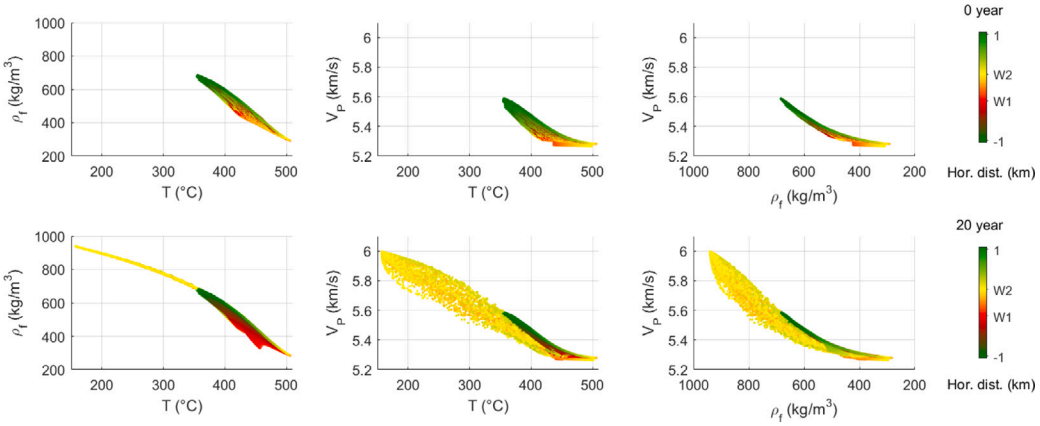

Fig. 6. Crossplot of fluid density (ρ_{fl}) and saturated rock compressional velocity (V_P) versus temperature (T) and V_P versus ρ_{fl} along the horizontal direction at 0 year and 20 year of cold re-injection. The colors red and yellow indicate the positions of the extraction (W1) and injection (W2) wells, respectively. (For interpretation of the references to color in this figure legend, the reader is referred to the web version of this article.)

located near well W1 (red points) where the extraction induces a decrease of the pore pressure and an increase of the temperature with the consequent variation of the density and the bulk modulus of the pore-fluid. However, the amount of changes is so small that it would be difficult to detect velocity variations with seismic monitoring.

3.3. 1-D evaluation of the reflection response

We process the data of the cold injection scenario. We investigate the reflection coefficients in the 1-D approximation, and analyze the seismic reflections from vertical discontinuities along the horizontal line, extracted at 5.5 km depth, where the fault is encountered at distance 0. This approach is not substitutive of the 2D full-waveform modeling, and is used to evaluate the trends in the observable seismic variations during the cooling phase. The reflection coefficients are therefore not representative of local anomalies or diffractions, but they are a measure of the contrast between zones with different physical properties for normal incidence reflections. The investigation is similar to the ideal reflectivity analysis by a log in a horizontal well, when passing from the left to the right side of a model of vertical layers. It is used to verify the order of magnitude of the reflection amplitude that can be expected for the variation of the temperature and pressure properties due to injection. Given the one-dimensional V_P velocity and ρ_m density profiles, the reflection response is calculated versus distance as

$$R_i = \frac{I_{i+1} - I_i}{I_{i+1} + I_i}, \tag{12}$$

where $I_i = V_{Pi}\ \rho_{mi}$ is the acoustic impedance of the ith element of the 1D array discretized every 5 m. Fig. 11 shows the profile of the P-wave reflection coefficients after 5 and 15 years of injection. Apart from a peak at the zero-distance, that represents the variation of the fault properties with respect to the background medium, the reflection coefficients are of the order of ±(0.007–0.0085), which would corresponds to a change of about 1.5–1.7% in the acoustic impedance.

We can observe the variation in the coefficients with the expansion of the reflection zone with increasing injection time. These values would make it possible, in favorable conditions, to seismically monitor, at regular time intervals, the geothermal reservoir, when cold fluid is re-injected. The reflection coefficients calculated in the case of isothermal re-injection are about 500 times weaker, making the seismic monitoring more difficult.

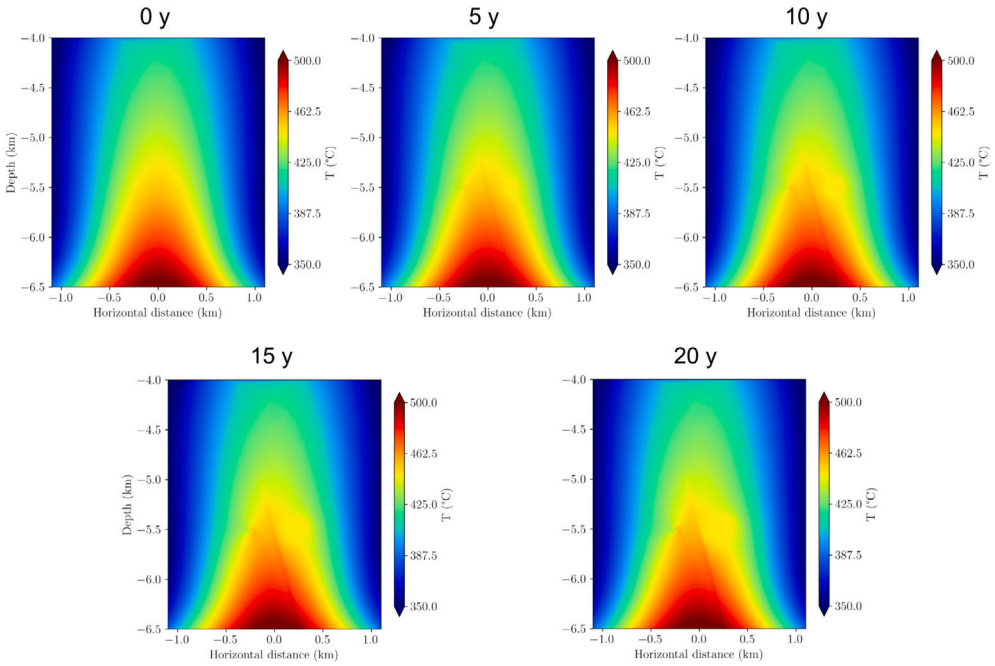

Fig. 7. Temperature models with 5-years step during 20 years of isothermal re-injection.

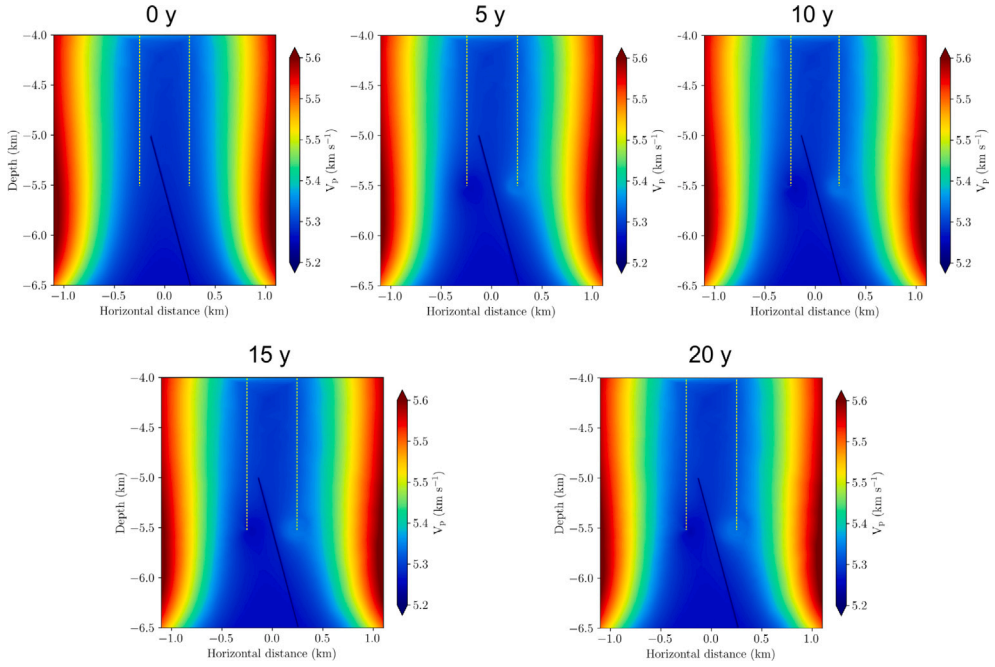

Fig. 8. Compressional phase-velocity models with 5-years step during 20 years of isothermal re-injection. Yellow lines indicate the position of the wells. (For interpretation of the references to color in this figure legend, the reader is referred to the web version of this article.)

3.4. Seismic waveform simulation

We calculate 2D synthetic wavefields to simulate the long term active seismic monitoring and to evaluate the trends in the observable seismic variations during the re-injection phases. We calculate the numerical propagation in the same area analyzed in the previous sections, neglecting the fault to better focus on the detectability of temperature changes during the injection. The 2D model is discretized with 5 m sided squared pixels, the source is a Richer wavelet with a peak frequency of 75 Hz. We simulate the single well seismic acquisition in the extraction well (W1) with a horizontal force as point source at 5.5 km depth and a vertical receiver line in the same well. In this configuration we calculate the time-lapse seismic profile. The simulation algorithm allow us to compute the snapshots of the wavefields, which are useful for the interpretation of the seismograms. Fig. 12 show the snapshots at the (x, z)-plane of the horizontal particle velocity (v_x), extracted at 100 ms and 140 ms at initial time and after 10 and 20 years during the cold re-injection exploitation, superimposed on the analytic compressional velocity models of Fig. 4. It is possible to observe how the signal is deformed when the wavefield meet a change of impedance crossing the cooled area. Similarly, we calculate the snapshots in the isothermal re-injection scenario and we report in Fig. 13 the results at initial time and after 20 years of isothermal re-injection. We note that the wavefield is almost unmodified during the exploitation. Fig. 14

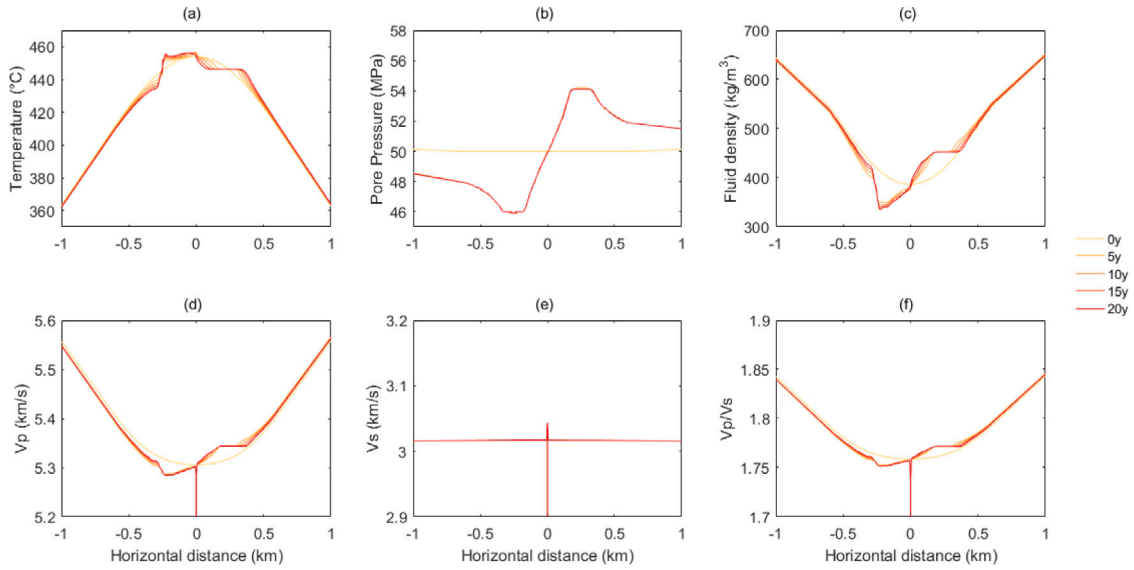

Fig. 9. 1D profiles of (a) temperature, (b) pore pressure, (c) pore-fluid density, saturated rock (d) compressional and (e) shear wave velocities and (f) V_P/V_S ratio, extracted along the horizontal line at the bottom-hole depth, 5.5 km. The data are calculated every 5 years during the isothermal re-injection.

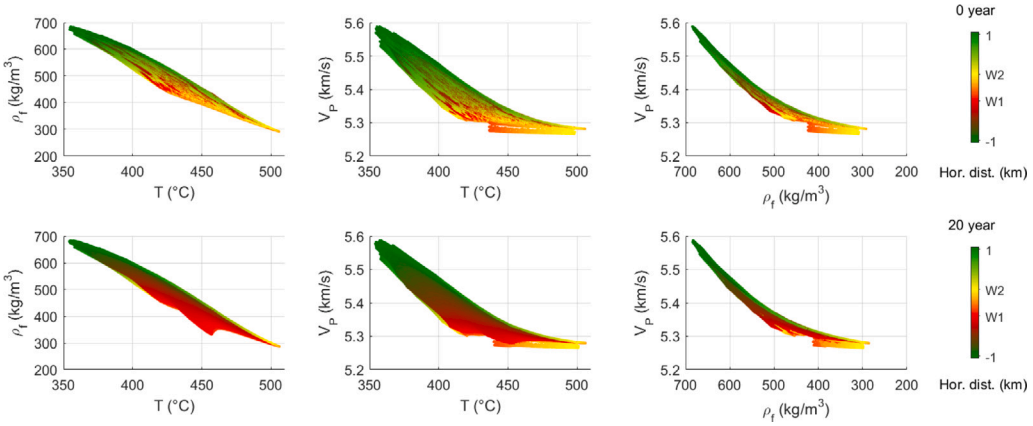

Fig. 10. Crossplot of fluid density (ρ_{fl}) and saturated rock compressional velocity (V_P) versus temperature (T) and V_P versus ρ_{fl} along the horizontal direction at 0 year and 20 year of isothermal re-injection. The colors red and yellow indicate the positions of the extraction (W1) and injection (W2) wells, respectively. (For interpretation of the references to color in this figure legend, the reader is referred to the web version of this article.)

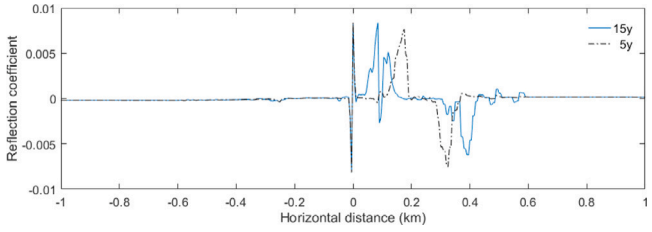

Fig. 11. P-wave reflection coefficients during the cold re-injection at 5 and 15 years.

shows examples of single-well vertical profiles simulated at the initial time and after 20 years of cold re-injection. Here we plot the vertical particle velocity component recorded in the well. We can observe the variation in the reflected events after long period of cold re-injection.

3.5. TLSP basic relations

We process the data simulated with the single well time-lapse-seismic profile (TLSP) geometry with the source and the receiver at the same fixed depth (5.5 km) in the production well (W1), sited at lateral position with respect to the injection zone. In this geometry we use the horizontal particle velocity receiver component to better visualize the P events, and neglect moveouts for sources and receivers located at different depths. Fig. 15a and b show the simulated signals before and after removal of stationary events, respectively. The separation is calculated by a using median filter on five adjacent traces, corresponding to a time lapse period of two years. The data after the separation highlight the evolution of the area interested by the seismic properties variations. This effect is graphically shown by the scheme of Fig. 15b. We define Δy the injection time interval in years, Δx (m) the lateral spatial shift of the horizontal distance and Δt the two-way seismic time increment in seconds. The lateral expansion rate (m/year) is given by

$$E_R = \frac{\Delta x}{\Delta y}. \tag{13}$$

The apparent velocity of the event representing the reflection front relocation in Fig. 15 is

$$V_A = \frac{\Delta y}{\Delta t}, \tag{14}$$

where V_A is a dimensionless quantity expressed in years/s. Assume for the unperturbed front (i.e., the front before the cold zone) a medium of seismic velocity V (m/s). For the spatial shift in relation to the variation

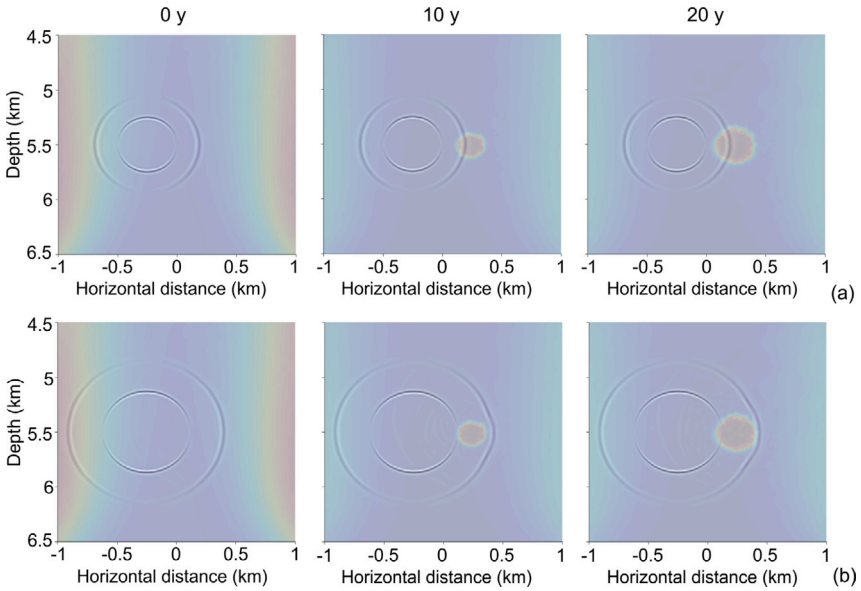

Fig. 12. Snapshots of the horizontal particle velocity component at (a) 100 ms and (b) 140 ms. The field has been computed at the (x, z)-plane every five years during the cold re-injection. The snapshots are superimposed on the analytic compressional velocity models of Fig. 3.

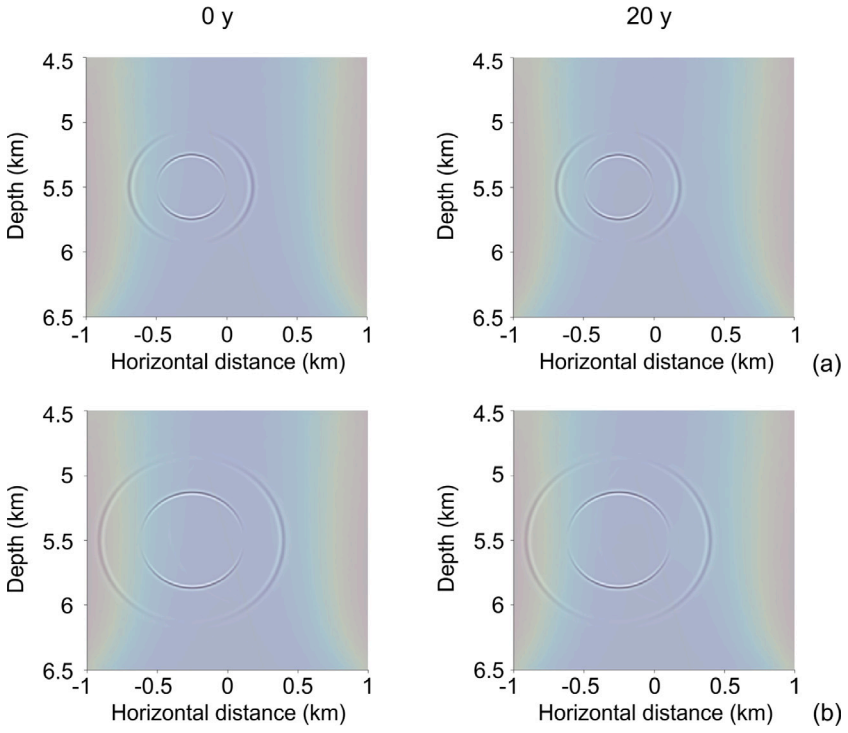

Fig. 13. Snapshots of the horizontal particle velocity component at (a) 100 ms and (b) 140 ms. The filed has been computed at the (x, z)-plane at initial time and after 20 years of isothermal re-injection. The snapshots are superimposed on the analytic compressional velocity models of Fig. 8.

of the reflection arrival time, we have

$$V = \frac{2\Delta x}{\Delta t}, \tag{15}$$

where we take into account that Δt is in two-way time. Combining previous equations we obtain

$$V_A = \frac{V}{2E_R}. \tag{16}$$

Assume maximum signal frequency f (Hz). Let ΔY be the injection time sampling interval (time between subsequent acquisitions). Similar to conventional vertical VSP, the aliasing condition for the apparent velocity representation is

$$\Delta Y = \frac{V_A}{2f}, \tag{17}$$

or using Eq. (16)

$$\Delta Y = \frac{V}{4E_R f}. \tag{18}$$

Eq. (18) tell us the sampling interval, i.e., the injection time interval for the measurement of the TLSP signals without aliasing conditions. This interval is function of the maximum signal frequency f, of the medium velocity V and of the expected expansion rate E_R.

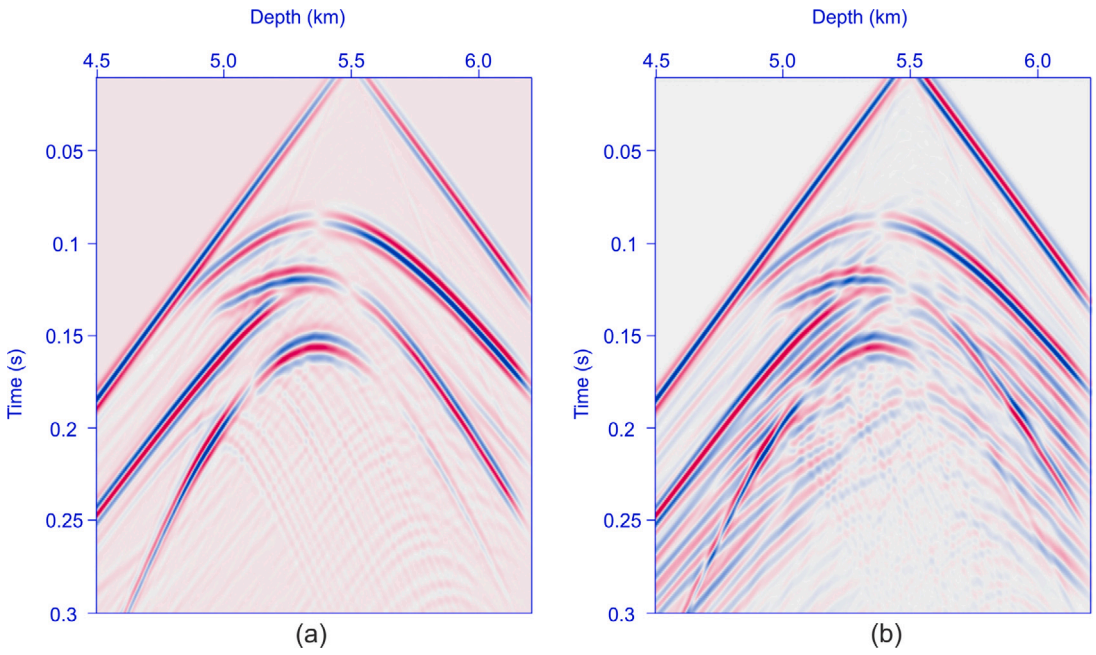

Fig. 14. Examples of single-well vertical profile (vertical particle velocity component) simulated in the single well acquisition layout at (a) 0 years and (b) after 20 years of cold re-injection.

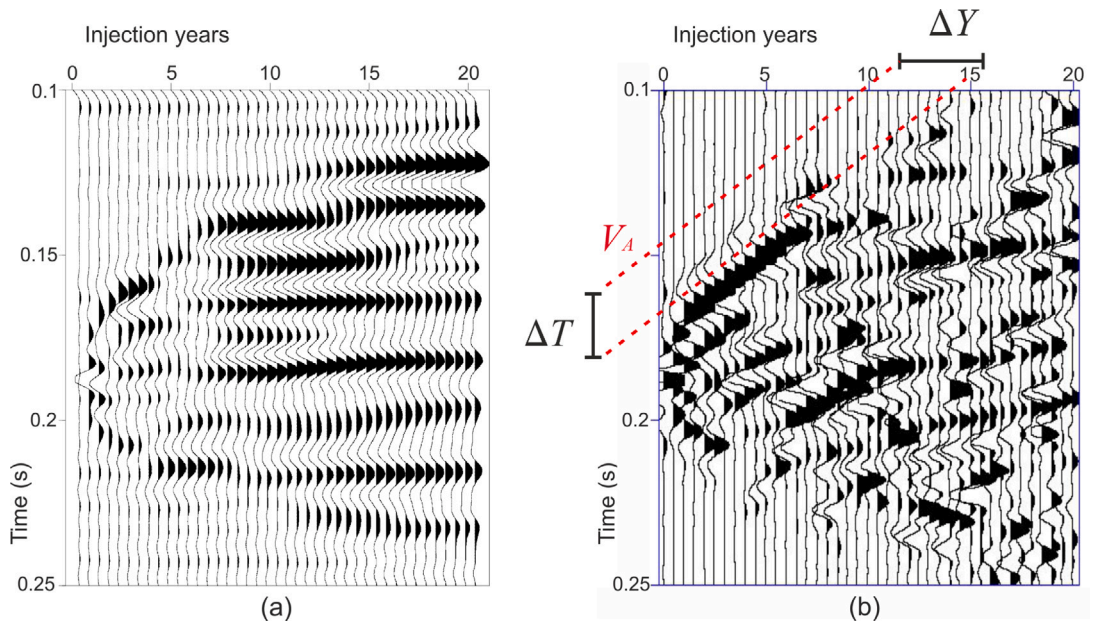

Fig. 15. Time-lapse signals, (a) before removing stationary events (b) residuals obtained after removal of stationary events. Concept of time-lapse seismic profile (TLSP) by measurements in well at repeated injection times. As an example, the traces are calculated every year from 0 to 20 years. ΔY is the injection time interval (years), ΔT the two-way seismic time interval (s), V_A is the apparent velocity.

As an example, assume for simplicity a medium of unperturbed compressional velocity $V = 4000$ m/s. Assume a wavefront expansion rate (here the sign is not relevant) $E_R = 20$ m/year, corresponding to 500 m in 25 years, and a maximum signal frequency $f = 100$ Hz. From Eq. (18) we obtain $\Delta Y = 0.5$ years.

Fig. 16 shows the results obtained by computing a synthetic seismogram with source and receiver at 5.5 km depth in the production well W1, every 0.5 years, from 0 to 20 years of injection. Fig. 16a represents the total TLSP wavefield obtained after removal of the stationary-reflection events in the time-lapse domain during the cold injection. Fig. 16b shows the corresponding result obtained during the isothermal injection. In the first scenario (a) the result is much clearer and of easier interpretation, while in (b) the result is noisier and of difficult interpretation.

Note that the wavefields represented in these figures show seismic waveforms, the signal of a single trace, evolving in the injection-time domain measured in years, and not the evolution of a physical wavefield in the space time domain. The next trace is not obtained by the spatial propagation of a same physical seismic wave, but represents its evolution in the time lapse domain, obtained by its repetition.

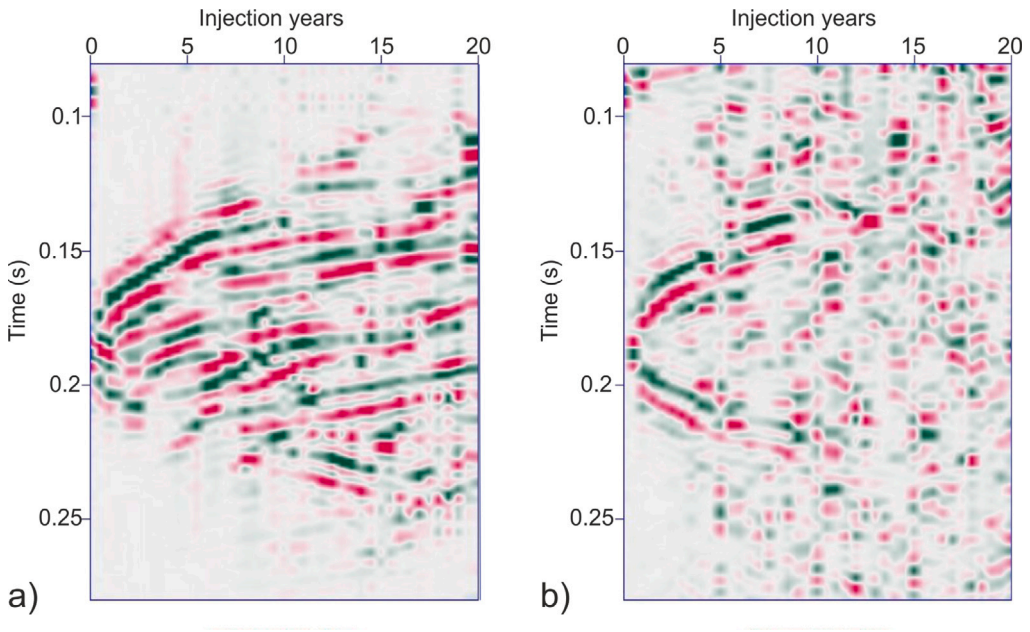

Fig. 16. Time-lapse examples calculated every 0.5 years from 0 to 20 years during cold re-injection. The signals are residuals obtained after removal of stationary events. (a) Wavefields in the cold injection scenario, and (b) wavefields in the isothermal injection scenario. Displayed signals are normalized trace-by-trace. In both panels, clear in (a) and noisy in (b), we can observe backward-moving (apparent updip) and forward moving (apparent downdip) time-lapse wavefronts.

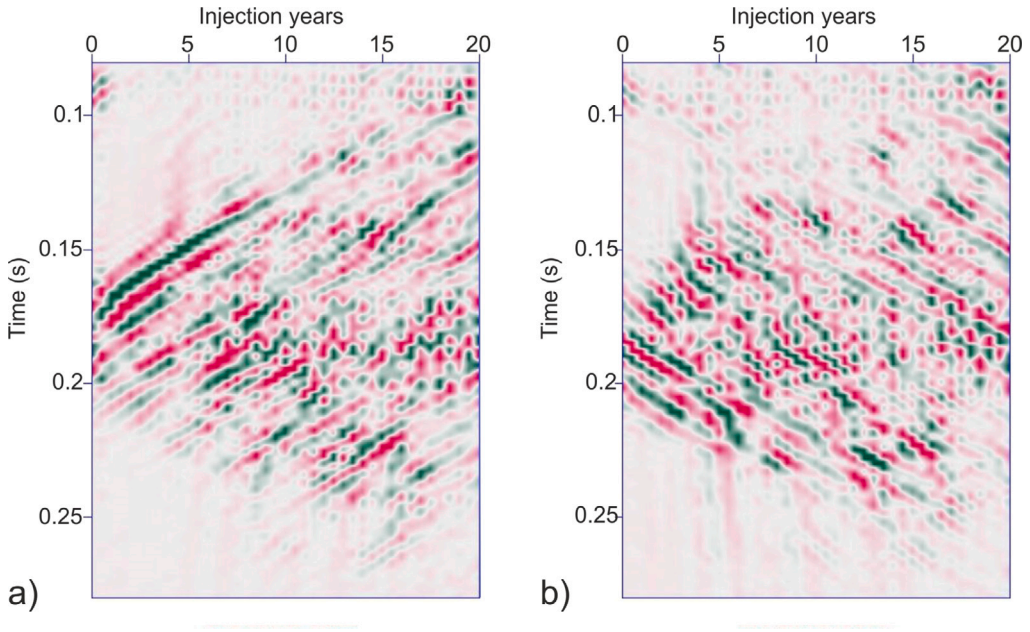

Fig. 17. The total TLSP wavefield of Fig. 16a (cold injection scenario) is separated in (a) backward wavefront approaching the source–receiver position as injection time (years) increases, and (b) forward wavefront with increasing distance as the injection time (years) increases.

Similar to conventional VSP, the repetition of the time-lapse (TL) measurements makes it possible to identify events with different 'wavefields' intended in the TL sense, representing the evolution of fronts at which reflections are generated. Fig. 16a, and also Fig. 16b, show events with different slopes.

The upgoing front, as the injection time increases, corresponds to approaching the source–receiver location, i.e., the point of observation of reflections when the reflection times are shorter. In other words, as the injection time increases the point of reflection moves close to the source–receiver location so that the reflection times are shorter. We call this front as backward. The downgoing front as the injection time increases correspond to fronts with increasing distance from the observation point, say forward. With appropriate TL sampling, these events can be separated by processing, similar to VSP wavefield separation. Fig. 17 shows (a) the separated *backward* field, and (b) the separated *forward* field, by dip filters, from the total field of Fig. 16a. Although the background model is smooth, the estimated reflection coefficients due to the temperature variation are not smooth. They change in position and also amplitude. This creates a variation effect in the results obtained with the time-lapse traces sampled every 0.5 years

in the injection time. To evidence reflections, stationary events masking reflections have been removed by median filters and the traces are normalized. This is a first result obtained with a single source–receiver position. In the course of the same simulation multiple shot-receiver gathers have been obtained with array of receivers. We expect that a multichannel processing of these data will further improve the imaging results, however this is beyond the scope of this paper. The difference between these fronts represent the expansion of the zone perturbed by injection, and is a basis for imaging the perturbed zone. We observe in the intermediate *expansion* zone of Fig. 16a internal events with different slopes, which can convey interesting information on the inner part of the perturbed are.

4. Discussions

This work studies the effects on the saturated formation seismic properties of a long term exploitation in a supercritical geothermal reservoir in the two possible extreme scenarios of cold and isothermal re-injection. Starting from the results of a THM modeling (Parisio et al., 2019), that define the temperature and stress conditions of the reservoir and the thermophysical properties of the geothermal fluid, we calculate the seismic properties of the saturated host rock. The seismic model at the initial time is homogeneous, apart from the presence of the fault and we calculate the seismic properties variations during the 20 years of exploitation. We firstly evaluate the effect of stress and temperature reservoir conditions on the drained host rock using the Arrhenius material constants of glassy basalt samples (Violay et al., 2012) to calculate the viscosity at the bottom-hole depth. We observe that the seismic properties fluctuations are mainly related to the thermophysical characteristics of the pore fluid. We calculate the velocity models during the exploitation with 5 years step and we observe that while in the case of isothermal injection the seismic properties fluctuations due only to the injection are too small to be seismically detected, the cold injection scenario can be seismically monitored.

A novel method is proposed to seismically monitor the evolution during the long term fluid injection. A key point is the ability of the method to observe the seismic variations caused by injection (e.g., Angerer et al., 2002). The analysis shows that weak reflection coefficients can be expected and used for monitoring in the case of cold re-injection. In the plane-wave normal-incidence approximation we neglect frequency-dependent effects (Quintal et al., 2011). The observability of the variations in the synthetic data depends on several aspects, such as S/N conditions and statistical presence of other reflection coefficients (Painter et al., 1995), that can mask the time-lapse events. An example is the fault-reflection at distance zero in Fig. 11.

To focus on the seismic response in the injection area at depth, we study the time lapse effect in the interwell area by single well imaging approach, with source and receiver in the production well. For some aspects, the approach is similar to vertical seismic profiling (VSP) (Hardage, 1992). This assumes the repeatability of the time-lapse borehole acquisitions, to collect a dense sequence of measurements sufficient to effectively process the reflection signals from the wavefronts induced by injection. We simulate the single well acquisition in the extraction well with six months step during the 20 years of cold re-injection exploitation and we can follow the growth of the anomalous area through the identification of the reflection events. The ability of the method to separate the signal and noise with arrays of single well imaging (SWI) sources and receivers is matter of future investigations in more complex seismic environments. In future developments, other time-lapse methods can use the seismic results of this study for imaging, such as crosswell imaging and inversion of time delays in transmitted waves sensitive to the variation in the seismic velocity model (Borges et al., 2020; Ajo-Franklin et al., 2013; Vasco et al., 2014), or VSP measurements by active sources at the surface.

This work analyzes a generalized case scenario that includes features common to many reservoirs. The methodology presented provides a useful reference approach that can be applied to specific geological conditions. Geothermal reservoirs are usually affected by a high degree of uncertainty about precise geological and thermal conditions (e.g., Ebigbo et al., 2016), mainly due to data accessibility issues for deep reservoirs and difficulties in upscaling laboratory results to in-situ conditions. The methodology we propose can provide a useful tool to constrain the geological uncertainty by combining seismic response to geomechanical simulations and can provide a powerful basis for inversion tool development. Aspects such as difficulties to repeat the time-lapse measurements in the boreholes and to perform measurements in high-pressure and high-temperature wells are not addressed in this analysis (e.g., Bertani et al., 2018). Some of these issues may be overcome by novel emerging technologies, such as new borehole tools, new thermal-resistant technology by fiber optic, signal redatuming methods such as seismic interferometry (Poletto et al., 2011) in case of difficulty to utilize permanent sources in the wells. Borehole noise fields can also be an issue, depending on the recording conditions, nature of wavefield components and on the distance of the investigated SWI target from the well. Nevertheless, the analysis demonstrates by simulation the feasibility of monitoring for the collection of time lapse seismic profiles, aimed at reconstructing the properties of the area perturbed by injection.

5. Conclusion

In this study we evaluate the possibility of seismic monitoring a supercritical geothermal reservoir during long-term cold and isothermal re-injections. We calculate the variations of the saturated rock seismic properties caused by the injection and we conclude that the cold case can be seismically monitored, while the changes are too small in the case of isothermal injection to be seismically detected. We conclude that, for melt-free supercritical geothermal systems the variations of the fluid properties induced by temperature changes dominate the seismic response of the reservoir. In case of geothermal exploitation in presence of temperature changes, seismic methods can be used to successfully monitor the spatial variations of the temperature in the reservoir during long-term exploitation.

CRediT authorship contribution statement

Biancamaria Farina: Conceptualization, Methodologies, Software, Data curation, Writing – original draft, Writing – review & editing. **Francesco Parisio:** Conceptualization, Software, Data curation, Writing – review. **Flavio Poletto:** Conceptualization, Formal analysis, Writing – review.

Declaration of competing interest

The authors declare that they have no known competing financial interests or personal relationships that could have appeared to influence the work reported in this paper.

Acknowledgments

Francesco Parisio acknowledges funding from the European Union's Horizon 2020 Research and Innovation Program through the Marie Sklowdowska-Curie Individual Fellowship ARMISTICE, Spain under Grant Agreement No. 882733.

Appendix. Table of model properties

Host rock petrophysical properties
Dry rock bulk modulus $K = 40$ GPa
Dry rock shear modulus $G = 24$ GPa
Biot's coefficient $\alpha = 0.5$
Solid phase bulk modulus $K_s = 80$ GPa
Solid phase density $\rho_s = 2700$ kg m^{-3}
Porosity $\phi = 0.01$
Fault petrophysical properties
Dry rock bulk modulus $K = 13.3$ GPa
Dry rock shear modulus $G = 8$ GPa
Biot's coefficient $\alpha = 1.0$
Reservoir thermal properties
Porous solid specific heat capacity $c_s = 950$ J kg^{-1} K^{-1}
Linear thermal expansion coefficient $\alpha_s = 1 \cdot 10^{-5}$ K^{-1}
Thermal conductivity $\lambda_s = 3\mathbf{I}$ W m^{-1} K^{-1}
Reservoir Arrhenius parameters
Stress exponent $n = 3.7$
Activation energy $E = 59$ kJ/mol
Material constant $A = 1.3 \cdot 10^{-9}$ (MPa^{-n}/s)
Numerical parameters for seismic waveform simulation
Pixel grid dimension 5 m
Source time function peak frequency 75 Hz
Time stepping $5 \cdot 10^{-4}$ s
Maximum propagation time 1.5 s

References

Ajo-Franklin, J., Peterson, J., Doetsch, J., Daley, T., 2013. High-resolution characterization of a CO2 plume using crosswell seismic tomography: Cranfield, MS, USA. Int. J. Greenh. Gas Control 18, 497–509.

Angerer, E., Crampin, S., Li, X.-Y., Davis, T.L., 2002. Processing, modelling and predicting time-lapse effects of overpressured fluid-injection in a fractured reservoir. Geophys. J. Int. 149 (2), 267–280.

Batzle, M., Wang, Z., 1992. Seismic properties of pore fluids. Geophysics 57 (11), 1396–1408.

Berryman, J.G., 1999. Origin of Gassmann's equations. Geophysics 64 (5), 1627–1629.

Bertani, R., Henrik, B., Stefan, B., Andrea, D., Magnus, H., Massimo, L., Adele, M., Roar, N., Wolfgang, R., Luca, S., the DESCRAMBLE Science Technology Team, 2018. The first results of the DESCRAMBLE project. In: Proc. of the 43rd Workshop on Geothermal Reservoir Engineering. In: SGP-TR-213, Stanford University, Stanford, California.

Borges, F., Landrø, M., Duffaut, K., 2020. Time-lapse seismic analysis of overburden water injection at the Ekofisk field, southern North Sea. Geophysics 85 (1), B9–B21.

Carcione, J., Farina, B., Poletto, F., Qadrouh, A., Cheng, W., 2020. Seismic attenuation in partially molten rocks. Phys. Earth Planet. Inter. 309, 106568.

Carcione, J., Helle, H., Gangi, A., 2006. Theory of borehole stability when drilling through salt formations. Geophysics 71 (3), F31–F47.

Carcione, J., Poletto, F., 2013. Seismic rheological model and reflection coefficients of the brittle–ductile transition. Pure Appl. Geophys. 170 (12), 2021–2035.

Carcione, J., Poletto, F., Farina, B., Craglietto, A., 2014. Simulation of seismic waves at the earth's crust (brittle–ductile transition) based on the Burgers model. Solid Earth 5 (2), 1001–1010.

Carcione, J., Poletto, F., Farina, B., Craglietto, A., 2017. The Gassmann–Burgers model to simulate seismic waves at the earth crust and mantle. Pure Appl. Geophys. 174 (3), 849–863.

Castro, R.R., Gallipoli, M.R., Mucciarelli, M., 2008. Crustal Q in Southern Italy determined from regional earthquakes. Tectonophysics (ISSN: 0040-1951) 457 (1), 96–101. http://dx.doi.org/10.1016/j.tecto.2008.05.022, https://www.sciencedirect.com/science/article/pii/S004019510800245X.

Chabot, L., Henley, D.C., Brown, R.J., Bancroft, J., 2001. Single-well imaging using the full waveform of an acoustic sonic. In: SEG Technical Program Expanded Abstracts 2001. Society of Exploration Geophysicists, pp. 420–423.

de Franco, R., Petracchini, L., Scrocca, D., Caielli, G., Montegrossi, G., Santilano, A., Manzella, A., 2019. Synthetic seismic reflection modelling in a supercritical geothermal system: An image of the K-horizon in the Larderello field (Italy). Geofluids 2019.

Ebigbo, A., Niederau, J., Marquart, G., Dini, I., Thorwart, M., Wolfgang, R., Pechnig, R., Ruggero, B., Christoph, C., 2016. Influence of depth, temperature,and structure of a crustal heat source on the geothermal reservoirs of tuscany: numerical modelling and sensitivity study. Geotherm. Energy http://dx.doi.org/10.1186/s40517-016-0047-7.

Elders, W., Fridleifsson, G., Albertsson, A., 2014. Drilling into magma and the implications of the Iceland Deep Drilling Project (IDDP) for high-temperature geothermal systems worldwide. Geothermics 49, 111–118.

Farina, B., Poletto, F., Mendrinos, D., Carcione, J.M., Karytsas, C., 2019. Seismic properties in conductive and convective hot and super-hot geothermal systems. Geothermics 82, 16–33.

Fornberg, B., 1987. The pseudospectral method: Accurate representation of interfaces in elastic wave calculations. Geophysics 53, 625–637.

Gangi, A.F., 1983. Transient and steady-state deformation of synthetic rocksalt. Tectonophysics 91 (1–2), 137–156.

Gurevich, B., Brajanovski, M., Galvin, R.J., Müller, T.M., Toms-Stewart, J., 2009. P-wave dispersion and attenuation in fractured and porous reservoirs – poroelasticity approach. Geophys. Prospect. 57 (2), 225–237. http://dx.doi.org/10.1111/j.1365-2478.2009.00785.x.

Han, D.-h., Batzle, M.L., 2004. Gassmann's equation and fluid-saturation effects on seismic velocities. Geophysics 69 (2), 398–405.

Hardage, B.A., 1992. Crosswell Seismology & Reverse VSP, Vol. 1. Geophysical Press.

Hornby, B.E., 1989. Imaging of near-borehole structure using full-waveform sonic data. Geophysics 54 (6), 747–757.

Jaya, M.S., Shapiro, S.A., Kristinsdóttir, L.H., Bruhn, D., Milsch, H., Spangenberg, E., 2010. Temperature dependence of seismic properties in geothermal rocks at reservoir conditions. Geothermics 39 (1), 115–123.

Jusri, T., Bertani, R., Buske, S., 2019. Advanced three-dimensional seismic imaging of deep supercritical geothermal rocks in Southern Tuscany. Geophys. Prospect. 67 (2v), 298–316v.

Kolditz, O., Bauer, S., Bilke, L., Böttcher, N., Delfs, J.-O., Fischer, T., Görke, U.J., Kalbacher, T., Kosakowski, G., McDermott, C., et al., 2012. Opengeosys: An open-source initiative for numerical simulation of thermo-hydro-mechanical/chemical (thm/c) processes in porous media. Environmental Earth Sciences 67 (2), 589–599.

Kosloff, D., Reshef, M., Loewenthal, D., 1984. Elastic wave calculations by the Fourier method. Bull. Seismol. Soc. Am. 74 (3), 875–891. http://dx.doi.org/10.1785/BSSA0740030875, Retrieved from https://doi.org/10.1785/BSSA0740030875.

Mavko, G.M., 1980. Velocity and attenuation in partially molten rocks. J. Geophys. Res.: Solid Earth 85 (B10), 5173–5189.

Montési, L.G., 2007. A constitutive model for layer development in shear zones near the brittle-ductile transition. Geophys. Res. Lett. 34 (8).

Painter, S., Beresford, G., Paterson, L., 1995. On the distribution of seismic reflection coefficients and seismic amplitudes. Geophysics 60 (4), 1187–1194.

Parisio, F., Lehmann, C., Nagel, T., 2020. A model of failure and localization of basalt at temperature and pressure conditions spanning the brittle-ductile transition. J. Geophys. Res.: Solid Earth 125 (11), e2020JB020539.

Parisio, F., Vilarrasa, V., Wang, W., Kolditz, O., Nagel, T., 2019. The risks of long-term re-injection in supercritical geothermal systems. Nature Commun. 10 (1), 1–11.

Poletto, F., Farina, B., Carcione, J.M., 2018. Sensitivity of seismic properties to temperature variations in a geothermal reservoir. Geothermics 76, 149–163.

Poletto, F., Farina, B., Carcione, J.M., Böhm, G., Mendrinos, D., Jousset, P., Pinna, G., Barison, E., 2019a. GEMex project, Deliverable 5.4: Report on seismic modeling. Retrieved from http://www.gemex-h2020.eu/index.php?option=com_content&view=article&id=12&Itemid=114&lang=en.

Poletto, F., Farina, B., Carcione, J.M., Pinna, G., 2019b. Analysis of seismic wave propagation in geothermal reservoirs. In: European Geothermal Congress EGC, Extended Abstract.

Poletto, F., Petronio, L., Farina, B., Schleifer, A., 2011. Seismic interferometry experiment in a shallow cased borehole using a seismic vibrator source. Geophys. Prospect. 59 (3), 464–476.

Quintal, B., Schmalholz, S.M., Podladchikov, Y.Y., 2011. Impact of fluid saturation on the reflection coefficient of a poroelastic layer. Geophysics 76 (2), N1–N12.

Ranalli, G., 1995. Rheology of the Earth. Springer Science & Business Media.

Reinsch, T., Dobson, P., Asanuma, H., Huenges, E., Poletto, F., Sanjuan, B., 2017. Utilizing supercritical geothermal systems: a review of past ventures and ongoing research activities. Geotherm. Energy 5 (16).

Solomon, S.C., 1972. Seismic-wave attenuation and partial melting in the upper mantle of north america. J. Geophys. Res. 77 (8), 1483–1502.

Vasco, D., Daley, T.M., Bakulin, A., 2014. Utilizing the onset of time-lapse changes: A robust basis for reservoir monitoring and characterization. Geophys. J. Int. 197 (1), 542–556.

Violay, M., Gibert, B., Mainprice, D., Evans, B., Dautria, J.-M., Azais, P., Pezard, P., 2012. An experimental study of the brittle-ductile transition of basalt at oceanic crust pressure and temperature conditions. J. Geophys. Res.: Solid Earth 117 (B3).

Watanabe, N., Abe, H., Okamoto, A., Nakamura, K., Komai, T., 2021. Formation of amorphous silica nanoparticles and its impact on permeability of fractured granite in superhot geothermal environments. Sci. Rep. 11 (1), 1–11.

Watanabe, N., Numakura, T., Sakaguchi, K., Saishu, H., Okamoto, A., Ingebritsen, S.E., Tsuchiya, N., 2017. Potentially exploitable supercritical geothermal resources in the ductile crust. Nat. Geosci. 10, 140–144.